

Journal of Biomedical Optics

BiomedicalOptics.SPIEDigitalLibrary.org

Phantom-based evaluation of near-infrared intracranial hematoma detector performance

Jianting Wang
Jonathan Lin
Yu Chen
Cristin G. Welle
T. Joshua Pfefer

Phantom-based evaluation of near-infrared intracranial hematoma detector performance

Jianting Wang,^{a,*} Jonathan Lin,^a Yu Chen,^b Cristin G. Welle,^{a,c} and T. Joshua Pfefer^a

^aU.S. Food and Drug Administration, Center for Devices and Radiological Health, Silver Spring, Maryland, United States

^bUniversity of Maryland, Fischell Department of Bioengineering, College Park, Maryland, United States

^cUniversity of Colorado, Department of Neurosurgery and Bioengineering, Aurora, Colorado, United States

Abstract. Near-infrared spectroscopy (NIRS) is emerging as a rapid, low-cost approach for point-of-care triage of hematomas resulting from traumatic brain injury. However, there remains a lack of standardized test methods for benchtop performance assessment of these devices and incomplete understanding of relevant light–tissue interactions. We propose a phantom-based test method for systems operating near the 800-nm oxy-/deoxy-hemoglobin isosbestic point and implement it to evaluate a clinical system. Semi-idealized phantom geometries are designed to represent epidural/subdural, subarachnoid, and intracerebral hemorrhages. Measurements of these phantoms are made with a commercial NIRS-based hematoma detector to quantify the effect of hematoma type, depth, and size, as well as measurement repeatability and detector positioning relative to the hematoma. Results indicated high sensitivity to epidural/subdural and subarachnoid hematomas. Intracerebral hematomas are detectable to a maximum depth of ~ 2.5 cm, depending on thickness and diameter. The maximum lateral detection area for the single-emitter/single-collector device studied here appears elliptical and decreases strongly with inclusion depth. Overall, this study provides unique insights into hematoma detector function and indicates the utility of modular polymer tissue phantoms in performance tests for emerging NIRS-based cerebral diagnostic technology. © The Authors. Published by SPIE under a Creative Commons Attribution 4.0 Unported License. Distribution or reproduction of this work in whole or in part requires full attribution of the original publication, including its DOI. [DOI: 10.1117/1.JBO.24.4.045001]

Keywords: near-infrared spectroscopy; standardization; hematoma detection; traumatic brain injury; light–tissue interaction; tissue phantoms.

Paper 180267RR received May 14, 2018; accepted for publication Mar. 20, 2019; published online Apr. 15, 2019.

1 Introduction

Traumatic brain injury (TBI) affects up to 2% of the population per year.¹ Among TBI patients, a common sequela is the development of an intracranial hematoma, which presents in 25% to 45% of severe TBI cases and 3% to 12% of moderate TBI cases.^{1,2} The mortality rate for patients with hematoma is high: 12% to 30% for epidural hematoma³ and 40% to 60% for subdural hematoma.^{1,2} Early detection and surgical evacuation of intracranial hematomas are fundamental management principles.¹ However, the current standard diagnosis relies on CT or MRI scans that are available only upon admission to the hospital, and often occurring hours to days following injury.⁴

To enable early identification of intracranial hematomas for military medicine and civilian emergency response, portable point-of-care devices based on near-infrared spectroscopy (NIRS) have been developed and commercialized. Several studies have indicated that these devices are capable of high sensitivity and specificity for *in vivo* detection of hematomas larger than 3.5 mL and located within 2.5 cm of the tissue surface.^{5–8} Clinical systems for hematoma detection typically use wavelengths near the 800-nm oxy–deoxy-Hb isosbestic point, due to the insensitivity of this spectral region to variations in blood oxygenation. However, NIRS devices have incorporated different algorithms and design characteristics that may lead to differences in clinical performance. For example, source–detector (S–D) geometry^{9,10} can impact penetration depth. Furthermore, some

NIRS devices use multiple S–D separation distances along with numerical routines to reduce the impact of chromophores in superficial layers (e.g., melanin absorption and bruising), which can confound brain tissue measurements. Given the intricacies of determining clinical testing of these devices, benchtop performance tests can act as valuable tools for system evaluation and intercomparison.

Phantom-based test methods, such as those developed for established imaging modalities (e.g., ultrasound and x-ray computed tomography),^{11,12} enable objective, quantitative, and consistent device testing based on well-characterized materials. Standardization of such approaches can facilitate technological advancement, regulatory clearance, quality assurance during manufacturing, consistency during clinical use, and recalibration. In recent years, there have been significant strides toward development of standardized test methods for biophotonic technologies, such as optical coherence tomography, fluorescence imaging, and NIRS-based oximeters. Given recent progress in NIRS-based hematoma detectors, there is an increasing need for well-validated, phantom-based test methods for this technology as well.¹³

A limited number of NIRS device phantoms simulating the head and brain have been developed and implemented for performance testing. Zhang et al.¹⁴ created two phantoms: (a) a single-layer phantom fabricated with polyester resin phantom doped with titanium oxide powder and India ink that incorporated a glass tube filled with whole blood 1.35 cm under the phantom surface to mimic a hematoma and (b) a two-layer phantom, in which the top layer had optical properties (OPs) simulating extracerebral tissues and was varied in thickness

*Address all correspondence to Jianting Wang, E-mail: jianting.wang@fda.hhs.gov

and a bottom layer representing a hematoma region. In both cases, a 1 optical density (OD) filter was placed on top of the phantom to simulate hair and skin absorption. To accommodate a hemispherical detection system, Riley et al.⁹ used a 7-cm-diameter cylindrical resin phantom with high absorption inclusions (5 and 10 times the background matrix absorption) at different depths to simulate intracranial hematomas. Additionally, a clinical study⁵ noted that phantom models of intracranial hematomas had been used to determine that hematomas of 3.5-mL volume located within 2.5 cm of the brain surface were detectable; however, no description of the phantoms was provided.⁵ Liquid phantoms have also been a popular choice due to their more easily adjustable OPs and overall flexibility in design;¹⁵ however, they are not stable over time, reducing the repeatability of experiments. The solid phantoms used in prior studies have not incorporated scalp, skull, cerebrospinal fluid (CSF), and brain structures nor do they mimic the wide, flat geometry of many superficial, trauma-induced hematomas.

The purpose of this study is to advance standardization of performance test methods for NIRS hematoma detectors. Toward this end, our goals included developing a set of robust, modular phantoms from solid polymers that model multiple physiologically relevant hematoma variations, then implementing the phantoms to test a commercial hematoma detection system.

2 Methods

2.1 Phantom Design

In this study, we created a multilayer head phantom based on physiologically realistic specifications that incorporates a range of hematoma classifications. We considered several distinct types of intracranial hematomas, including epidural, subdural, subarachnoid, and intracerebral. The first three are more commonly induced through moderate to severe TBI. Based on prior CT imaging studies, we have attempted to identify idealized structures to represent each of these four hematoma

types.¹⁶ This approach is in line with phantoms described in standards for established medical imaging modalities that use idealized inclusions to represent tissue structures for basic performance testing^{17,18} that can be easily replicated. The specific designs selected are described in Fig. 1 and Table 1, and include (1) epidural/subdural, (2) subarachnoid, and (3) intracerebral hematomas. Our model of the head includes four base layers: scalp, skull, CSF, and cerebral tissue (comprised of multiple identical layers). For the epidural and subdural hematoma, a blood-simulating layer spanning the full width of the phantom is included between the skull and CSF layers. For the subarachnoid hematoma, a CSF-diluted blood layer is represented in the space between the skull and cerebral tissue. Although it is known that subarachnoid hematomas are diluted by CSF,¹⁹ the representative dilution rate or hemoglobin concentrations are not readily available in literature. We used 60% blood concentration as a worst-case estimation based on CT (x-ray computed tomography) numbers reported previously for subarachnoid hematomas²⁰ and subdural hematomas.²¹ Intracerebral hematomas are simulated using disks within the cerebral tissue.

2.2 Phantom Fabrication

Multilayer phantoms were fabricated using two primary matrix materials—polydimethylsiloxane (PDMS) and polyurethane (PU). PDMS (Dow Corning Sylgard 184, Auburn, Michigan),

Table 1 Hematoma geometries incorporated into phantoms.

Thickness (mm)	Hematoma volume (mL)					
	1	1.8	3	5	10	30
5-cm disk	0.5	0.9	1.5	2.5	5.1	15.3
8.5-cm disk	—	—	0.5	0.9	1.8	5.3

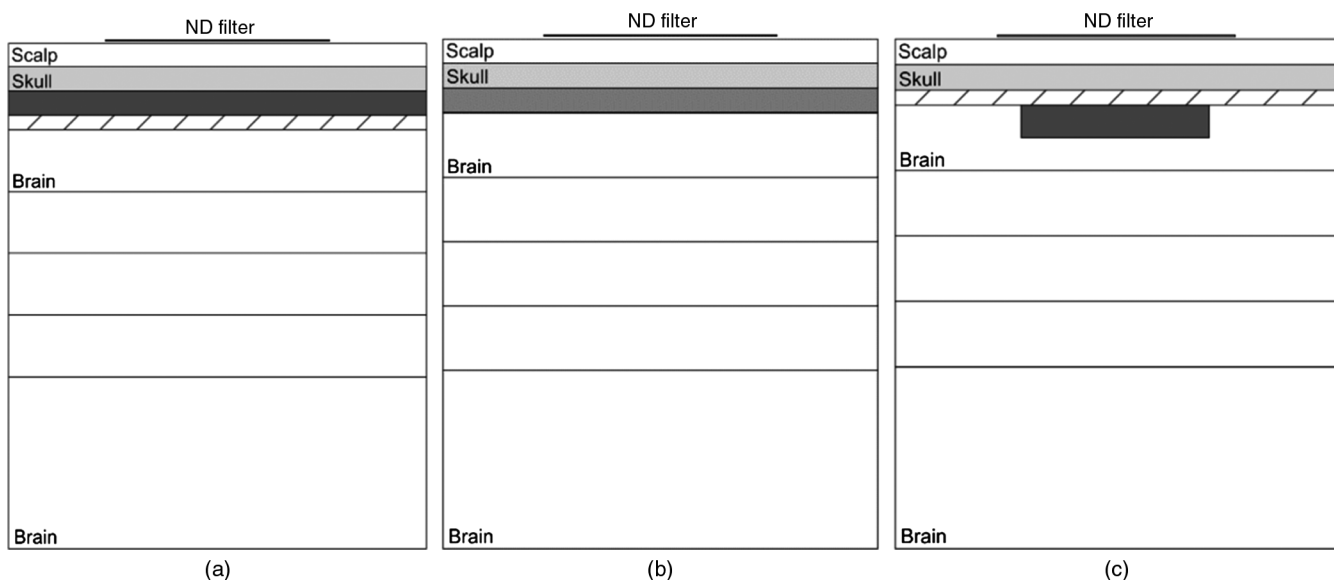


Fig. 1 Schematic of phantoms representing (a) epi/subdural, (b) subarachnoid, and (c) intracerebral hematomas. Dark-shaded regions in (a) and (c) represent blood, light-shaded region in (b) represents blood-CSF mixture; hashed regions represent CSF layer. Layer thicknesses: 3 mm for scalp, 5 mm for skull, and 3 mm for CSF.

which has an index of refraction (n) of 1.4, was used for all layers except for the skull layer.¹⁷ Titanium dioxide particles (TiO₂, anatase powder, Sigma-Aldrich, St. Louis, Missouri) and India ink were used to tune the scattering coefficient and absorption coefficient of PDMS layers. Stock solution of Sylgard 184 base with titanium dioxide or India ink at high concentration was prepared by mixing and sonicating using a probe tip sonicator (Q500 Sonicator, Qsonica, Newtown, Connecticut) for 10 h. To allow heat generated from the sonication to dissipate, the sample was placed in a room temperature water bath, and the sonication was done with a 10-s on and 20-s off cycle. The stock solutions were added to PDMS base at desired concentration and mixed with curing agent at 10:1 ratio. The mixture was poured into molds and kept in vacuum for an hour to remove air bubbles.

The molds for intracerebral hematomas were polystyrene petri dishes of 5- or 8.5-cm diameter. For brain layers, a glass petri dish of 12.5-cm diameter was used. For brain layers containing hematoma, the cured hematoma phantom was placed at the bottom of the mold, and uncured PDMS representing brain was poured over the hematoma at desired volume (calculated by measured weight) and placed in an oven at 75°C for 4 h to cure. It should be noted that a meniscus shape is formed due to surface tension along the lateral edge of the phantom when PDMS is cured with the surface open to air. Thus, for thinner layers—i.e., epi and subdural hematoma, scalp, and CSF layers (3-mm thickness)—a different molding approach was used to ensure uniform layer thickness. A 15-cm-diameter petri dish was used as the mold. Near the side of the petri dish cap, three-dimensional (3-D) printed spacers at desired thickness were glued to the dish. PDMS mixture was poured into the petri dish cap, and the petri dish bottom that has a slightly smaller diameter was placed on top of the spacers. The mold was then put in the oven to cure the PDMS. For thin hematomas (<1-mm thick), a spin coater (WS-650MZ-23NPP Spin Coater, Laurell Technologies Corporation, North Wales, Pennsylvania) running at 500 RPM for 30 s was used to apply a thin PDMS layer (~0.2-mm thickness) to the underside of a polystyrene petri dish, before curing in the oven. Layers were applied and cured repeatedly until the desired thickness hematoma was achieved, determined by weight.

PU (WC781, BJB Enterprises, Tustin, California; $n = 1.47$) was used to make the layer mimicking skull as it is not easily compressed as PDMS.¹⁸ The same titanium oxide particles were added to PU as scattering agent, and plastic black colorant (BPC, M-F Manufacturing Co., Fort Worth, Texas) was used as absorbing agent. The molding and curing methods used were the same as fabrication of the PDMS layers, except for different ratio between part A and part B of the PU (1:0.85) and time for curing (~16 h). For intracerebral hematoma phantoms [Fig. 1(c)], the CSF layer was fabricated first, and then the skull and scalp layers were successively poured on top and cured, resulting in a single component containing the scalp/skull/CSF layers, minimizing assembly effort and any air gap between the layers.

2.3 Evaluating the Impact of Hemoglobin Oxygenation

Measurements of the hematoma detector's light source with a high sensitivity spectrometer (QE65 Pro Scientific Grade Spectrometer, Ocean Optics, Dunedin, Florida) indicated a center wavelength of 805 nm and a bandwidth of 2 nm

(full-width-half-maximum). Thus, the device's output is close to the near-infrared (NIR) oxy-/deoxy-hemoglobin isosbestic point at 800 nm. In a prior study, Zhang et al.¹⁴ noted that a wavelength of 805 nm "is suitable for hematoma detection since... the signal detected will not be affected by differences in oxygen." However, no data were provided to support this assertion. The actual isosbestic point is at 798 nm, while at 805 nm the μ_a of oxy-Hb (4.6 cm⁻¹) is 18% greater than that of deoxy-Hb (3.9 cm⁻¹).²² Thus, variations in saturation might introduce some degree of confounding effect in detected signals. To assess the robustness of the hematoma detector to blood oxygenation, we measured a phantom incorporating hemoglobin solutions with different saturation levels. Specifically, we used a 3-D printed phantom with $\mu'_s = 10$ cm⁻¹, as measured with a spectrophotometer and inverse adding doubling (IAD) software. The phantom was designed with a disk-shaped void space (10 mL, 8.5-cm diameter, and 1.8-mm thick) and a removable top layer (1.0 mm thick) above the void space. The phantom included a removable 1-mm-thick top layer above the void space. A commercially available hemoglobin solution (Multi-4 CO-Oximeter Control, Level 2, Hb concentration = 13.8 g/dL, Instrumentation Laboratory Co., Bedford, Massachusetts) was used to represent the hematoma. The saturation level of the solution was changed by adding yeast and validated through CO-oximetry (Avoximeter 4000, Accriva diagnostics, San Diego, California). Measurements were performed for saturation values ranging from 3% to 99%.

2.4 Optical Property Characterization

For phantoms of each tissue type, a 1-mm-thick sample of 4-cm diameter was made from the same batch of uncured mixture for OP measurement. The total reflectance and transmittance were measured using a 150-mm integrating sphere and spectrophotometer (Lambda 1050 UV/VIS/NIR, Perkin Elmer, Inc. Waltham, Massachusetts), and IAD software²³ was then used to calculate the absorption (μ_a) and reduced scattering coefficients (μ'_s). The OPs used in the phantoms are shown in Table 2 and are based largely on clinical frequency-domain NIRS measurements in the adult head from a prior study.²⁴

2.5 Near-Infrared Spectroscopy Measurements

The clinical hematoma detector used in this study (Fig. 2) evaluates the presence of hematomas based on spatial variations in signal attenuation. The device has one illumination fiber and one collection fiber; each has a diameter of 2 mm and the fiber separation distance is 4 cm. While the device's primary function involves providing the user with a warning indicator when differences in signal attenuation increase beyond the threshold level, it also provides quantitative attenuation data for each measurement in terms of OD. Unless otherwise indicated, the measurements in our study were performed with the detector

Table 2 Thickness and OPs of tissue phantom layers²⁴

	Scalp	Skull	CSF	Brain	Hematoma
Thickness (mm)	3	5	3	70	Varied
μ'_s (/mm)	1.06	1.33	—	0.51	1.8
μ_a (/mm)	0.016	0.013	—	0.02	0.36

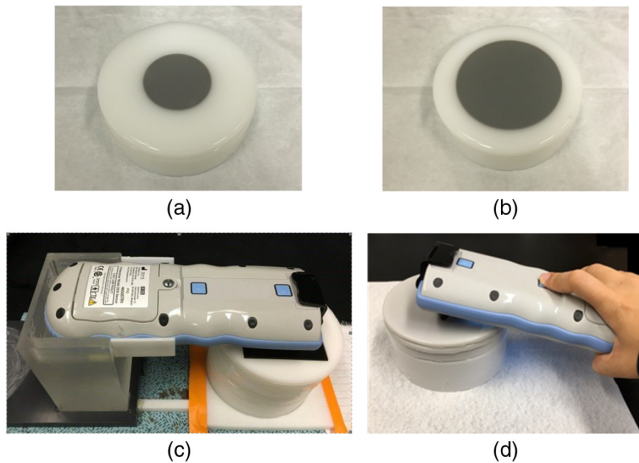


Fig. 2 Photographs of phantom layers incorporating (a) 5- and (b) 8.5-cm-diameter hematoma-simulating inclusions, as well as the (c) hematoma detector on its scaffold and (d) during a handheld measurement.

mounted on a custom-designed scaffold to ensure that pressure was consistent, yet light enough to minimize compression of the top phantom layer. Change in optical density (ΔOD) was calculated by measuring normal and hematoma phantoms with the detector.

$$\Delta OD = \log_{10} \frac{I_N}{I_H}, \quad (1)$$

where I_N is the measured reflectance intensity for normal tissue and I_H is the measured intensity for a hematoma region. The threshold for hematoma detection used by this device is $\Delta OD > 0.2$.

2.6 Measurement Repeatability

A variety of factors can impact the repeatability of hematoma detection during phantom testing and real-world use. Improved understanding of these factors can help to optimize test methods and facilitate practical interpretation of the results. The repeatability of phantom measurements was evaluated by acquiring normal brain phantom OD data under six different scenarios. Although the hematoma detector is intended to be used as a handheld device, for standard performance testing, it is desirable to separate user-induced variability from other sources of error. Therefore, a custom holder was fabricated to fix the detector position relative to the phantom and ensure a small, yet consistent level of pressure. The weight of the detector on the phantom was measured as 190 g (1.86 kN). Both handheld and holder-mounted measurements were performed for each of the following cases: (1) repeat acquisitions without moving the device, (2) removal and replacement of the device on the phantom between acquisitions, and (3) removal and restacking of phantom layers between acquisitions.

2.7 Effect of Hematoma Morphology on Detectability

Variations in hematoma detectability due to changes in morphology were explored by varying the geometry of epidural/subdural, subarachnoid, and intracerebral hematoma phantoms (Fig. 1). For the epi/subdural phantom geometry and subarachnoid geometry, the hematoma thickness was varied from 1 to

4 mm. To assess device sensitivity to intracerebral hematomas, the depth, diameter, and thickness of hematoma inclusions were varied. Specifically, hematoma depths of 0, 0.55, 1, 1.55, 2, and 3 cm below the CSF layer were measured, corresponding to total depths of 1.1 to 4.1 cm. At each depth, hematoma volumes of 3, 5, 10, and 30 mL were implemented. To achieve these volumes, inclusion thicknesses of 1.5, 2.5, 5.1, and 15.3 mm for the 5-cm-diameter hematoma, and 0.5, 0.9, 1.8, and 5.3 mm for the 8.5-cm-thick hematoma were used. For the 5-cm-diameter hematoma, two additional hematoma volumes were measured, 1 and 1.8 mL (with thicknesses of 0.5 and 0.9 mm), to better visualize thickness effects and provide similar thicknesses for comparison to the 8.5-cm-diameter hematomas. The ΔOD between normal phantoms and each individual hematoma case was quantified and compared.

2.8 Lateral Sensitivity

To elucidate the impact of lateral offset on hematoma detectability, a test method based on the intracerebral hematoma geometry (Fig. 1) was developed. Measurements were performed using four different phantom layers incorporating 5-cm-diameter hematomas shifted laterally from the center by 0, 1, 2, or 3 cm (Fig. 3). Two depth scenarios were studied: 0.0 and 0.55 cm below the CSF layer (1.1 or 1.65 cm below the phantom surface). Thus, measurements were made at seven locations in the X direction [along the S–D axis, as in Fig. 3(a)] and the Y direction [perpendicular to the S–D axis, as in Fig. 3(b)]. In all measurements, the detector was centered on the phantom as illustrated. Since the detector had an S–D separation distance of 4 cm, for all hematoma positions along the S–D axis [Fig. 10(a)] either the source, detector, or both fibers were positioned above the hematoma, we did not extend measurements to the point at which neither fiber was positioned over the hematoma ($X = 4.5$ cm) as limited by the diameter of the phantom. For displacements perpendicular to the S–D axis, however, the hematoma was below the S–D axis as long as the hematoma lateral offset was 2.5 cm or less.

2.9 Statistical Analysis

All measurements were repeated four times and the standard deviations are shown as error bars in figures. All statistical analysis was performed in Excel, using Excel Data Analysis tool box. Analyses performed include exponential/logarithmic regression with analysis of variance (ANOVA) outputs to evaluate correlation between two variables, and a paired sample t -test with null hypothesis in which the mean difference between two sets of data is zero.

3 Results

3.1 Effect of Hematoma Oxygenation

Measurements of phantoms containing hematoma-simulating inclusions filled with a human hemoglobin solution at different oxygen saturation (S_tO_2) levels showed small differences in ΔOD (Fig. 4). Saturation level appeared to exhibit minimal effect on signal attenuation, which is supported by p -value = 0.73 from regression analysis/ANOVA. These data confirm that the proximity of the illumination wavelength to the NIR isosbestic point provides insensitivity to oxygenation level, as stated by Zhang et al.¹⁴ Furthermore, it supports the validity

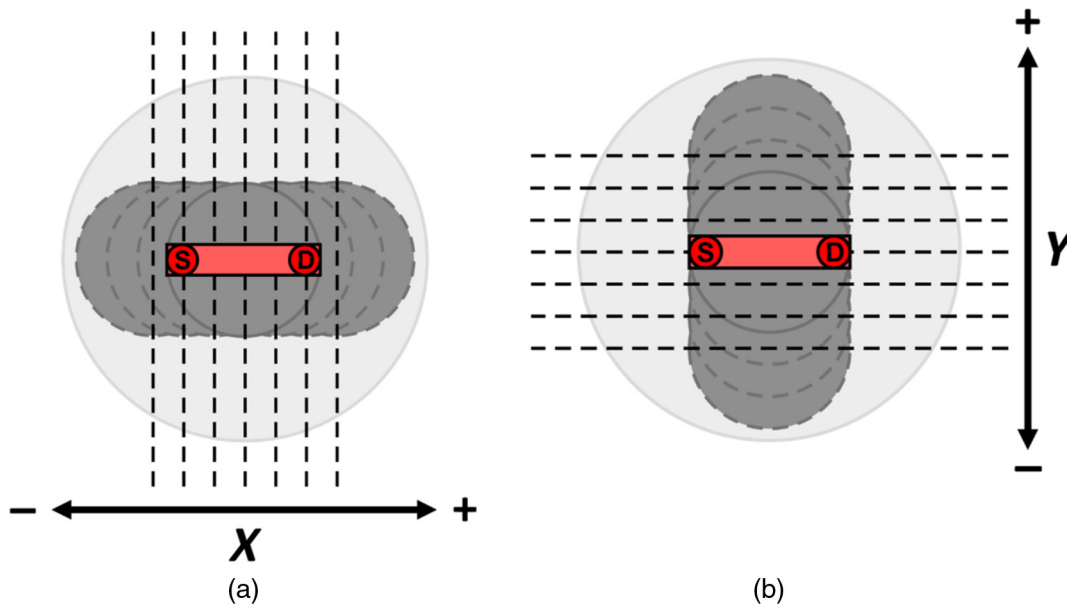


Fig. 3 Variations in hematoma inclusion position during lateral sensitivity measurements. Initially centered with the source and detector fibers, inclusions were repositioned either (a) along the S–D axis (X direction) or (b) perpendicular to this axis (Y direction). The hematoma inclusion was 5 cm in diameter, located 0 or 0.55 cm below the CSF layer; S–D separation distance was 4 cm.

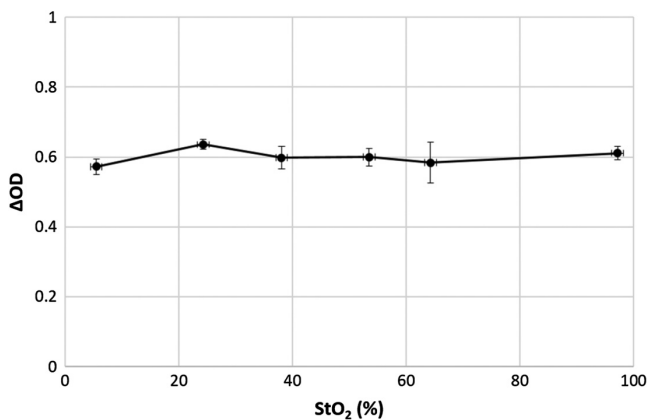


Fig. 4 Effect of hemoglobin oxygenation level (StO_2)—as measured by a CO-oximeter—on hematoma detector measurements.

of a phantom-based approach that involves a stable and neutral absorber rather than oxygenated and deoxygenated hemoglobin.

3.2 Measurement Repeatability

Results illustrating measurement variability based on the six measurement configurations described in Sec. 2 are shown in Fig. 5. For consecutive handheld measurements without any movement of the detector, the error level was moderately low, however, much greater than when the scaffold was used. When the detector was removed and reapplied to the phantom surface, variability increased by a factor of 3 to 4. Finally, when the phantom was restacked and the detector reapplied to the phantom, the standard deviation increased again by a factor of 2 or 3. These results indicate that using a scaffold may slightly reduce the variability of phantom measurements, and that variability overall was low, even when restacking of the phantom layers was considered.

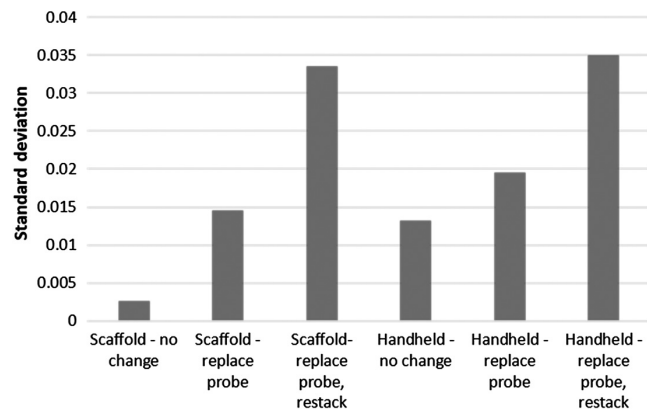


Fig. 5 Repeatability of hematoma detector OD measurements ($n = 5$) for four different acquisition protocols.

3.3 Visualization of Near-Infrared Light Distributions

To provide initial qualitative insights into light–tissue interactions, a mobile phone camera (based on a color CMOS sensor) with NIR blocking filter removed (Eigen Imaging, Inc., San Diego, California) was used to record videos during the measurement process. Images were acquired of the top/side [Fig. 6(a)] of the phantom, as well as below the hematoma layer for 0.55- and 3-mm-thick intracerebral hematomas (i.e., imaging bottom side of the phantom with the nonhematoma brain layers removed). It should be noted that if the image in Fig. 6(a) was normalized to the maximum value near the illumination fiber, the rapid decay in light intensity as a function of distance would preclude visualization of light in more distant regions. By manually controlling exposure, it was possible to visualize the wider light propagation pattern, although the region near the illumination fiber was saturated. In the other two figures, the effects of hematoma thickness on light attenuation

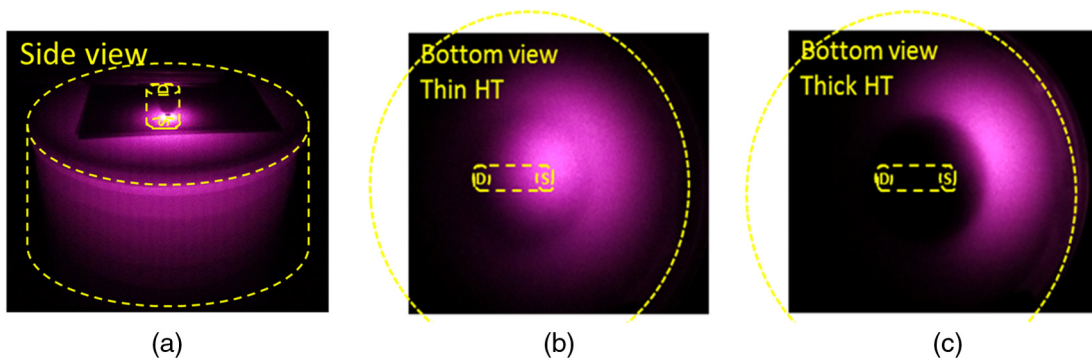


Fig. 6 Visualization of NIR light in the phantom during hematoma detector operation, as acquired from (a) above and to the side of the phantom; as well as directly below the hematoma layer for a 5-cm-diameter intracerebral hematoma [Fig. 1(c)] with thicknesses of (b) 0.5 and (c) 3 mm.

are illustrated. For the thinner hematoma [Fig 6(b)], significant attenuation has occurred, but some light that has penetrated directly below the illumination fiber is apparent. However, for the thicker hematoma [Fig 6(c)], only light that has diffused around the inclusion is visible.

3.4 Effect of Cerebrospinal Fluid Layer

As a test of the significance of the CSF layer on NIRS measurements, we compared attenuation levels for intracerebral hematomas with and without a 3-mm-thick CSF layer. Measurements were performed for two hematomas, 5-cm diameter with 5.1-mm thickness (10 mL volume) and 8.5-cm diameter with 5.3-mm thickness (30 mL volume), varying in depth from 0 to 3 mm below the CSF layer or skull layer when no CSF layer was present. Although adding/removing the CSF layer would change the depth of the hematoma from the phantom surface, since CSF layer is clear, it is not expected to attenuate the optical signal. Results (Fig. 7) showed greater ΔOD values for hematomas in phantoms without a CSF layer compared to those with a CSF layer—by up to 0.5 for 5-cm-diameter hematomas and up to 0.8 for 8.5-cm-diameter hematomas. As depth increased, the fractional impact of the CSF layer on attenuation by the hematoma remained roughly constant. A paired two-sample *t*-test resulted in *p*-values of 0.0001 and 0.0004 for 5- and 8.5-cm-diameter hematomas, respectively, showing that there is a statistically significant difference between the ΔOD values obtained with and without a CSF layer.

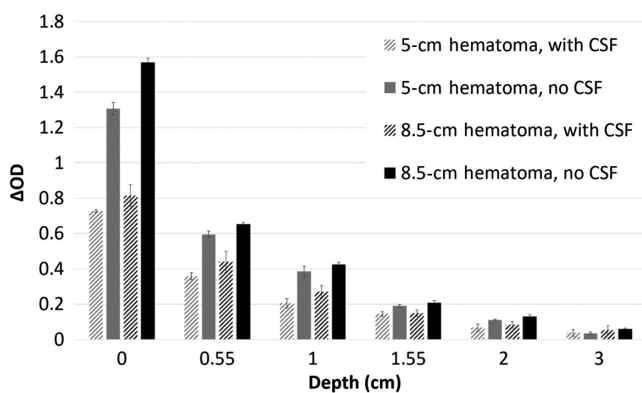


Fig. 7 Effect of CSF layer presence on system sensitivity to 5- and 8.5-cm-diameter intracerebral hematomas as a function of depth.

3.5 Epi/Subdural and Subarachnoid Hematoma Detection

Results were generated that illustrate the effect of hematoma type—epidural/subdural, subarachnoid, and intracerebral—on device sensitivity. A comparison of superficial hematomas—epidural/subdural and subarachnoid—is shown in Fig. 8. High sensitivity to all of these superficial hematomas cases was indicated, in that ΔOD values were consistently above 1.2. For epidural/subdural hematomas, no increase in ΔOD was seen beyond a thickness of 2 mm and a regression analysis indicated that overall, signals did not correlate strongly with inclusion thickness across the 1- to 4-mm depth range (logarithmic regression, $R^2 = 0.715$). For subarachnoid hematomas, signals increased with hematoma thickness up to 3 mm, and a stronger statistical correlation was shown (logarithmic regression, $R^2 = 0.996$). The limited correlation for epi/subdural hematomas was likely due to the strong attenuation of light as it propagated both into and out of the tissue, and the fact that little light could propagate laterally to the detection fiber in the superficial layers alone. As a result, the reflectance signal quickly approached the limit of the dynamic range of the device and showed a maximum ΔOD of ~ 2.3 .

3.6 Intracerebral Hematoma Detection

The effects of intracerebral hematoma depth, diameter, and thickness on detectability are presented in Fig. 9. Hematoma depth had perhaps the clearest impact, with exponential regressions of the attenuation (ΔOD) versus depth relationship producing R^2 values in the range of 0.97 to 0.99 for both 5- and 8.5-cm-diameter inclusions. By identifying where these

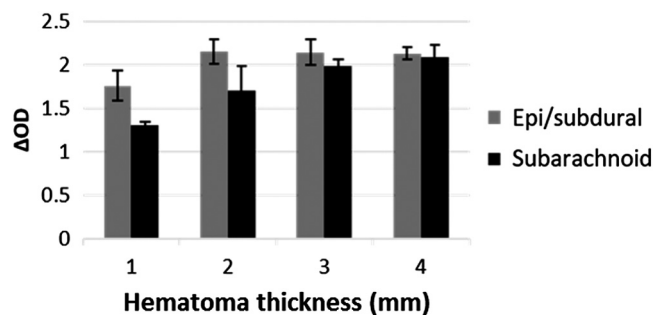


Fig. 8 NIRS system sensitivity to epi/subdural and subarachnoid hematomas over a range of hematoma thicknesses.

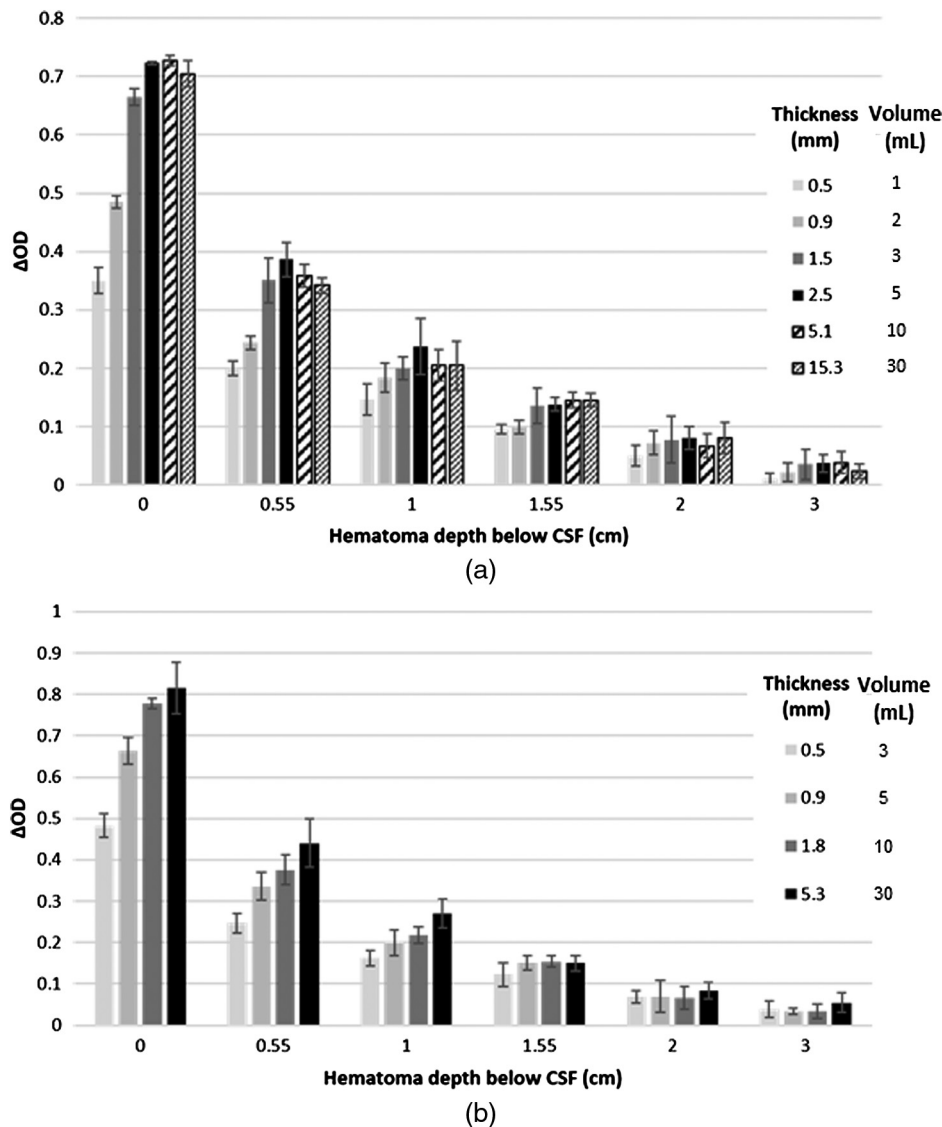


Fig. 9 Effect of volume/thickness and depth on detectability in intracerebral hematoma phantoms. Results are presented for hematoma diameters of (a) 5.0 and (b) 8.5 cm. Note that distance from phantom surface through CSF layer is 1.1 cm.

regression lines crossed the $\Delta OD = 0.2$ threshold, it was possible to estimate that maximum detection depth ranged from 0.6 to 1.2 cm (with increasing inclusion thickness) for the 5-cm hematoma cases tested and from 0.9 to 1.4 for the 8.5-cm cases. All hematomas deeper than 1.55 cm, as well as very thin hematomas at 1-cm depth, were not detectable ($\Delta OD < 0.2$). Therefore, since the bottom of the CSF layer was located 1.1 cm below the surface, the detection depth of the detector from the tissue surface was ~ 1.7 to 2.5 cm, depending on hematoma size.

The impact of hematoma thickness was also strong, over a limited range of values. For 5-cm-diameter hematomas, ΔOD increased until the thickness reached about 2.5 mm (10-mL volume), and regression analyses based on a logarithmic fit over this range showed relatively high R^2 values (0.98, 0.96, 0.97, 0.82, 0.64, and 0.85). For 8.5-cm-diameter hematomas, significant increases in ΔOD were seen up to thicknesses of 1.8 mm, and logarithmic regression also tended to show high R^2 values (0.83, 0.94, 0.99, 0.44, 0.85, and 0.81). The magnitude of attenuation changes with thickness decreased

rapidly with depth; as a result, the best regression fits were found for more superficial hematomas (e.g., $R^2 > 0.9$ for depths of 0 and 0.55). Additionally, for corresponding thicknesses, 8.5-cm-diameter hematomas showed greater ΔOD than those with a diameter of 5 cm (one-tailed, paired sample t -test produced a $p < 0.05$ over depths of 0 to 1.55 cm).

3.7 Lateral Variations in Sensitivity

Another key performance issue is how sensitivity is impacted by lateral positioning of the detector relative to the hematoma. The effect of positioning—both along and perpendicular to the S–D axis (as illustrated in Fig. 3)—is presented in terms of ΔOD (Fig. 10) for 5-cm-diameter hematomas. Results for positions along the S–D axis [Fig. 10(a)] indicated that ΔOD for the 0-cm depth hematoma decreased from a maximum of ~ 0.7 at the center position to 0.47 at a lateral offset of 3 cm in the positive X direction and to 0.39 in the negative X direction. For the deeper hematoma, the maximum ΔOD was 0.3, decreasing to 0.21 at a lateral offset of 3 cm. These results indicate that

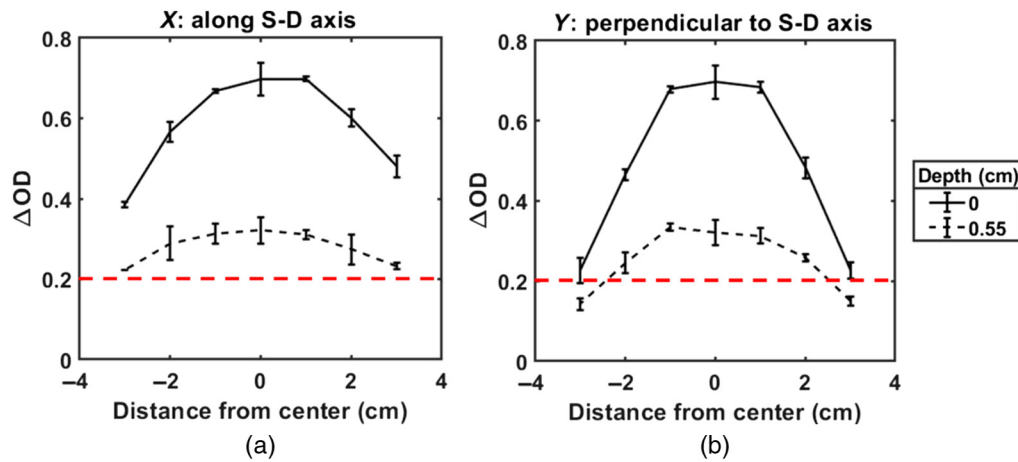


Fig. 10 Effect of device-hematoma lateral offset (a) along and (b) perpendicular to the S–D axis (as illustrated in Fig. 3). Results are presented for a 5-cm-diameter intracerebral hematoma located at depths of 0 and 0.55 cm below the CSF. The red dashed line indicates the detection threshold. Note that in (a), some part of the hematoma is directly below one of the fibers as long as the distance from the center is <4.5 cm, whereas in (b), some part of the hematoma is directly below the S–D axis as long as the distance from the center is <2.5 cm.

although superficial hematomas provided greater attenuation than deeper ones for all lateral positions, the magnitude of this difference decreases with lateral displacement. While both hematomas were in the detectable range for all positions in Fig. 10(a), results indicated that the deeper inclusion would only be detectable to X offsets of ± 3 cm and the superficial one to ± 4 cm. Thus, in practice, detection with this device would only be likely if a significant portion of the hematoma is positioned between the fibers. Additionally, our results indicated a slight asymmetry in the lateral sensitivity curve, with ΔOD appearing slightly larger when only the detection fiber was above the hematoma, as compared to when only the source fiber was above the hematoma (one-tailed, paired sample t -test: $p = 0.003$). The experiment was repeated by rotating the probe 180 deg to the phantom and the same asymmetry pattern depending on the hematoma location relative to S–D was observed, confirming that the trend is not due to inhomogeneity of phantom (data not shown). However, for the deeper hematoma, this effect was diminished to the point where it was not statistically significant (one-tailed, paired sample t -test: $p = 0.46$).

In the perpendicular offset scenario [Fig 10(b)], ΔOD remained relatively constant until beyond a 1-cm offset for both hematomas. Beyond this point, ΔOD showed a strong decrease with position for the more superficial hematoma, falling to near the detection threshold at 3 cm. For the deeper hematoma, ΔOD decreased from a maximum near 0.3 to 0.15 at 3-cm displacement. Although the deeper hematoma became undetectable when the S–D axis was no longer above the inclusion (2.5 cm from center), the superficial hematoma was still detectable for another 0.5 cm. Thus overall, the device's detection region appears elliptical in shape, slightly larger along the S–D axis than perpendicular to it, and decreasing strongly with lesion depth.

4 Discussion

In this study, we have addressed the lack of basic performance testing data and standardized test methods for infrared hematoma detectors operating near the 800-nm isosbestic region.

Specifically, we have developed, characterized, and implemented a set of phantoms for evaluating the sensitivity of these devices. Unlike prior phantom-based studies of hematoma detectors, these phantoms combined the use of (a) layered structures with generalized tissue-mimicking morphologies representative of epidural/subdural, subarachnoid, and intracerebral hematomas and (b) stable polymer matrices incorporating levels of chromophores and scatterers useful for measurements near the NIR oxy-/deoxy-hemoglobin isosbestic point. Overall, our approach is moderately biorealistic and task based, yet provides information regarding essential performance (e.g., penetration depth, hematoma morphology, etc.) and is simple enough to be readily reproduced. Measurements of these phantoms with a clinical hematoma detector have provided evidence of the utility of our approach, as well as a more thorough understanding of NIRS-based hematoma detector performance than provided in existing literature.

Several preliminary tests performed in this study helped clarify basic issues to guide development of our final phantoms. We showed that for a device operating close to the NIR isosbestic point, changes in hemoglobin oxygen saturation do not impact results significantly (Fig. 4), and thus, chromophores, such as India ink, which can be readily incorporated into a polymer matrix are suitable, provided that significant metHb is not present, which may develop over time.²⁵ We also showed that scaffold-based measurements could help reduce variability over a standard handheld approach; and then implemented this method to minimize error and more clearly elucidate basic trends in device performance (Fig. 5). An NIR-enabled mobile phone proved a highly useful tool for visualization of light propagation, helping to illustrate the device's temporal pulse structure as well as the rapid decay in signal intensity with lateral position and the impact of phantom depth and inclusion size (Fig. 6). Additionally, we performed measurements indicating that incorporating a CSF-simulating layer in the phantom reduces sensitivity to subarachnoid hematomas (Fig. 7). Similar measurements performed for intracerebral hematoma geometries showed a similar effect (data not presented). This finding corroborates the effect of CSF predicted by prior computational simulations.²³ Overall, the results of these preliminary tests have

not only been useful for development of best practices that are rigorous yet minimally burdensome but also have provided key insights into light–tissue interactions.

Results obtained with our phantom-based test methods provided confirmation of prior results as well as some quantitative insights into several aspects of clinical hematoma detector performance. Sensitivity to superficial hematomas, including sub/epidural and subarachnoid, was quite high with all thicknesses studied producing an attenuation change of $\Delta OD > 1.0$ (Fig. 8). This result is in good agreement with prior clinical data²⁶ indicating that ΔOD values for subdural hematoma were about twice as great as those for than intracerebral values (~ 0.85 versus 0.4). However, Robertson et al.⁵ indicated that clinical measurements of subarachnoid hemorrhages were highly variable, ranging from 0.03 to 0.86. This may be an indication that the mixing of blood with CSF fluid in the subarachnoid space—and the nonuniformity in the thickness of this layer—causes a lower and more variable hematoma absorption coefficient than simulated with our phantoms.

For intracerebral hematomas, the depth, thickness, and width of an inclusion all played a role in determining detectability. The degree of light attenuation by a hematoma decreased strongly with depth and, to a slightly lesser degree, increased with hematoma thickness (Fig. 9) for a few millimeters before leveling off. System sensitivity to the larger hematoma was slightly greater than the smaller hematoma for corresponding thicknesses. The maximum depth of detectable hematomas (based on a threshold of $\Delta OD = 0.2$) was in the 2- to 2.5-cm range below the phantom surface. For hematomas of ~ 3.5 mL, a maximum detection depth of ~ 2.1 cm was seen. This value is slightly less than the 2.5-cm detection depth found in prior clinical and phantom measurements.^{5,27}

The lateral range of detectability was explored in Fig. 10. These results indicate that the device can detect hematomas over a greater range along the S–D axis than perpendicular to the S–D axis. In general, superficial hematomas tended to be detectable as long as one of the fibers, or the S–D axis, was directly above some portion of the hematoma, whereas for deeper hematomas (0.55 cm below CSF), they were only detectable if the center of the device was directly above some portion of the hematoma. This limited spatial range is likely what led the authors of one clinical study to suggest that a key limitation of the technology was the illumination-detection configuration, which necessitated that the “location of the hematoma must be precisely determined” to obtain an accurate evaluation.²¹ Francis et al.⁸ presented phantom results for simulated hematomas at different depths that provide qualitative agreement with our finding that the lateral zone of detection was limited to regions directly below and between the source and detector fibers. However, this study focused primarily on the effect of S–D separation distance for inclusions of different shapes.

Although only one hematoma detector was tested in this study, many aspects of the phantom methods and procedures implemented here, such as the use of a flat absorber, the use of multilayer approach including CSF, and a modular phantom for evaluating device performance over a range of geometries, can be generalized to other devices, with or without modifications to accommodate other devices. While these results indicate the strong promise of our approach to provide standardized performance assessment, there are a number of issues that may represent fruitful areas of research in the future. Our results confirm that near-isosbestic wavelengths provide robustness to

changes in hemoglobin saturation that can help to simplify phantom design. However, viable approaches for hematoma detection may exploit other wavelengths, necessitating phantoms that can incorporate blood or blood-simulating chromophores.

Skin pigmentation level is a potential confounding factor on the performance of NIRS devices. Although the absorption of skin pigmentation would be canceled out when ΔOD is calculated by subtraction of the baseline, skin pigmentation may change the overall detectable depth, signal-to-noise ratio, and sensitivity. We are currently developing epidermal phantom layers for cerebral NIRS with varied pigmentation levels and intend to apply this approach to test the hematoma detector in the future.

Another limitation of our modular phantom approach is the variability caused by stacking of the multiple phantom layers. Compared to other hard materials such as PU, PDMS can be fabricated with very smooth surface; as it is elastic, it allows excellent contact between layers when pressed together. However, air gaps between layers that lead to increased noise are still possible, especially when layers are thin (e.g., < 3 mm). Approaches that require minimum restacking of phantom layers during use, with multiple thin layers cured to form thicker layers for stacking are desirable to minimize variability.

In the future, we intend to pursue development of biomimetic phantoms that provide more realistic results and represent variations in key properties across the patient population (e.g., phantom curvature, layer thicknesses, and OPs). Specifically, the use of 3-D printing approaches²⁸ may provide more accurate prediction of *in vivo* performance. It is also worth noting that test methods to address other potential confounding factors may be useful. For example, as indicated by Kessel et al.,⁷ “large subcutaneous haematomas, which are not uncommon in head injuries, may impede proper measurement of OD on the side of the haematoma.” Since test methods are not available to evaluate robustness to this or other biological factors that may degrade performance, additional study is warranted.

5 Conclusions

The current work provides insights into best practices for bench-top performance testing that can elucidate NIRS-based hematoma detector light–tissue interactions and facilitate product development and clinical translation. Results presented here also help to clarify the impact of tissue and device variables on hematoma detection, including hematoma geometry and lateral positioning. Furthermore, the objective, quantitative approaches described here provide a foundation for future standards addressing the use of optical technologies for NIRS-based cerebral diagnostics in hospital and point-of-care settings.

Disclosures

The authors have no relevant financial interests in this article and no potential conflicts of interest to disclose.

Acknowledgments

The authors gratefully acknowledge support for this research from FDA’s Medical Countermeasures Initiative Regulatory Science Program (MCM 301). The authors also acknowledge the support through Oak Ridge Institute for Science and Education (ORISE) program by Oak Ridge Associated Universities (ORAU).

Disclaimer

The opinions and conclusions stated in this paper are those of the authors and do not represent the official position of the Department of Health and Human Services. The mention of commercial products, their sources, or their use in connection with material reported herein is not to be construed as either an actual or implied endorsement of such products by the Department of Health and Human Services.

References

1. M. R. Bullock et al., "Surgical management of acute epidural hematomas," *Neurosurgery* **58**(Suppl. 3), S7–S15 (2006).
2. D. Thurman and J. Guerrero, "Trends in hospitalization associated with traumatic brain injury," *JAMA* **282**(10), 954–957 (1999).
3. S. C. Bir et al., "Incidence, hospital costs and in-hospital mortality rates of epidural hematoma in the United States," *Clin. Neurol. Neurosurg.* **138**, 99–103 (2015).
4. J. Silver, T. McAllister, and S. Yudofsky, *Textbook of Traumatic Brain Injury*, American Psychiatric Publishing, New York (2005).
5. C. S. Robertson et al., "Clinical evaluation of a portable near-infrared device for detection of traumatic intracranial hematomas," *J. Neurotrauma* **27**(9), 1597–1604 (2010).
6. S. Kahraman et al., "The accuracy of near-infrared spectroscopy in detection of subdural and epidural hematomas," *J. Trauma* **61**(6), 1480–1483 (2006).
7. B. Kessel et al., "Early detection of life-threatening intracranial haemorrhage using a portable near-infrared spectroscopy device," *Injury* **38**(9), 1065–1068 (2007).
8. S. V. Francis et al., "Screening for unilateral intracranial abnormalities using near infrared spectroscopy: a preliminary report," *J. Clin. Neurosci.* **12**(3), 291–295 (2005).
9. J. D. Riley et al., "A hematoma detector—a practical application of instrumental motion as signal in near infra-red imaging," *Biomed. Opt. Express* **3**(1), 192–205 (2012).
10. D. Nahman et al., "Devices and methods for detection of internal bleeding and hematoma," The United States Patent and Trademark Office, Hadasit Medical Research Services and Development Co, U.S. Patent No. US20150099980A1, (2015).
11. M. M. Goodsitt et al., "Real-time B-mode ultrasound quality control test procedures. Report of AAPM ultrasound task group No. 1," *Med. Phys.* **25**(8), 1385–1406 (1998).
12. C. H. McCollough et al., "The phantom portion of the American College of Radiology (ACR) computed tomography (CT) accreditation program: practical tips, artifact examples, and pitfalls to avoid," *Med. Phys.* **31**(9), 2423–2442 (2004).
13. A. I. Maas and G. Citerio, "Noninvasive monitoring of cerebral oxygenation in traumatic brain injury: a mix of doubts and hope," *Intensive Care Med.* **36**(8), 1283–1285 (2010).
14. Q. Zhang et al., "Study of near infrared technology for intracranial hematoma detection," *J. Biomed. Opt.* **5**(2), 206–213 (2000).
15. H. Wabnitz et al., "Performance assessment of time-domain optical brain imagers: a multi-laboratory study," *Proc. SPIE* **8583**, 85830L (2013).
16. T. H. Le and A. D. Gean, "Neuroimaging of traumatic brain injury," *Mt. Sinai J. Med.* **76**(2), 145–162 (2009).
17. A. Agrawal et al., "Multilayer thin-film phantoms for axial contrast transfer function measurement in optical coherence tomography," *Biomed. Opt. Express* **4**(7), 1166–1175 (2013).
18. T. Moffitt, Y. C. Chen, and S. A. Prahl, "Preparation and characterization of polyurethane optical phantoms," *J. Biomed. Opt.* **11**(4), 041103 (2006).
19. L. A. Hayman et al., "Pathophysiology of acute intracerebral and subarachnoid hemorrhage: applications to MR imaging," *Am. J. Roentgenol.* **153**(1), 135–139 (1989).
20. A. M. Boers et al., "Automatic quantification of subarachnoid hemorrhage on noncontrast CT," *Am. J. Neuroradiol.* **35**(12), 2279–2286 (2014).
21. M. G. Rao et al., "Dating of early subdural haematoma: a correlative clinico-radiological study," *J. Clin. Diagn. Res.* **10**(4), HC01–HC05 (2016).
22. S. A. Prahl, "Tabulated molar extinction coefficient for hemoglobin in water," 1999, <https://omlc.org/spectra/hemoglobin/summary.html>.
23. S. A. Prahl, M. J. van Gemert, and A. J. Welch, "Determining the optical properties of turbid media by using the adding-doubling method," *Appl. Opt.* **32**(4), 559–568 (1993).
24. J. Choi et al., "Noninvasive determination of the optical properties of adult brain: near-infrared spectroscopy approach," *J. Biomed. Opt.* **9**(1), 221–229 (2004).
25. W. G. Bradley, Jr. and P. G. Schmidt, "Effect of methemoglobin formation on the MR appearance of subarachnoid hemorrhage," *Radiology* **156**(1), 99–103 (1985).
26. C. S. Robertson, S. P. Gopinath, and B. Chance, "A new application for near-infrared spectroscopy: detection of delayed intracranial hematomas after head injury," *J. Neurotrauma* **12**(4), 591–600 (1995).
27. J. Leon-Carrion et al., "The Infrascanner, a handheld device for screening in situ for the presence of brain haematomas," *Brain Inj.* **24**(10), 1193–1201 (2010).
28. Y. Liu et al., "Biomimetic 3D-printed neurovascular phantoms for near-infrared fluorescence imaging," *Biomed. Opt. Express* **9**(6), 2810–2824 (2018).

Biographies of the authors are not available.